Resolving Global Internal Tides Reveals Fine-Scale Ocean Circulation

Badarvada Yadidya[1*], Brian K. Arbic[1,2], Edward D. Zaron[3],

Jay F. Shriver[4], Maarten C. Buijsman[5], Eric P. Chassignet[6],

Loren Carrère[7], Michel Tchilibou[7]

[1]Department of Earth & Environmental Sciences, University of Michigan, Ann Arbor, MI, USA.

[2]Research School of Earth Sciences, Australian National University, Canberra, ACT, Australia.

[3]College of Earth, Ocean, and Atmospheric Sciences, Oregon State University, Corvallis, OR, USA.

[4]Naval Research Laboratory, Stennis Space Center, MS, USA.

[5]Division of Marine Science, University of Southern Mississippi, Stennis Space Center, MS, USA.

[6]Center for Ocean-Atmospheric Prediction Studies, Florida State University, Tallahassee, FL, USA.

[7]Collecte Localisation Satellites, 31520 Ramonville-Saint-Agne, France.

[*]Corresponding author. Email: yadidyabadarvada@gmail.com

The new high-resolution Surface Water and Ocean Topography (SWOT) satellite is designed to reveal fine-scale ocean circulation, resolving the mesoscale and sub-mesoscale features that drive Earth's climate. Paradoxically, this unprecedented resolution is also hampered by a 'veil' of internal tides, which are now more prominent than ever. This observational noise, particularly its previously unpredictable, non-phase-locked component, has long hindered satellite altimetry. We address this challenge with a data-assimilative global ocean forecast model. Validated against SWOT data, our model demonstrates that this entire internal tide field is far more predictable than previously assumed. We present the first high-resolution maps of the non-phase-locked component, showing it often dominates the open-ocean signal. Our framework removes up to 59% more internal tide variance than current methods, recasting a major observational error into a largely predictable physical field. This breakthrough helps part the tidal veil, significantly advancing SWOT's ability to observe fine-scale ocean dynamics.

The ocean's ability to absorb heat and carbon, which regulates the pace of climate change, is governed by a turbulent circulation of eddies and filaments (*1, 2*). Observing these climate-critical features from space has long been thwarted by a fundamental obstacle: the internal tide. Generated by the interaction of barotropic (surface) tidal flows with undersea topography (*3, 4*), these kilometer-scale waves obscure satellite measurements. Their signals are often indistinguishable from the very circulation scientists need to measure. Internal tides are also a cornerstone of the global climate system in their own right. They propagate for thousands of kilometers (*5, 6*), driving a significant fraction of the diapycnal mixing that maintains ocean stratification (*7, 8*), and cascading energy down to small-scale turbulence (*9, 10*). Yet by masking the ocean's turbulent circulation, their energetic signature on the sea surface throws a persistent veil over our view of the planet's climate engine.

For over three decades, conventional nadir-altimetry satellites provided one-dimensional traces of the sea surface, restricting our view of its two-dimensional structure (*11, 12*). The recently launched Surface Water and Ocean Topography (SWOT) mission fundamentally changes this (*1, 13, 14*). By utilizing wide-swath radar interferometry, SWOT delivers the first high-resolution, two-dimensional maps of SSH, resolving ocean features down to scales of 5 km (*15, 16*).

This new capability, however, exposes a fundamental observational barrier. SWOT's high-resolution measurements also bring the energetic and complex internal tide field into sharp focus, making it difficult to distinguish climate-regulating, eddy-driven transport from transient tidal energy. This challenge stems from the tide's two-part nature. The first component, which is phase-locked (or coherent) with the astronomical tides, is predictable and has been robustly mapped (*6, 17–21*). The second, a non-phase-locked (or incoherent) component, has remained a critical blind spot. This component is highly variable, constantly modulated by shifting mesoscale eddies, wave-wave interactions, and stratification (*22–24*).

This non-phase-locked tide creates the fundamental ambiguity: its spatial scales and amplitudes are nearly identical to the very mesoscale features SWOT was designed to observe. The empirical correction atlases developed in the pre-SWOT era are therefore inadequate for this new challenge, as they only account for the predictable, phase-locked part (*25, 26*).

Here we resolve this observational impasse, demonstrating that the "unpredictable" non-phase-locked tide is, in fact, largely deterministic and predictable. Our approach leverages a key insight: since the non-phase-locked tide is modulated by the background circulation (*22–24*), a model that correctly simulates this circulation should also correctly simulate the non-phase-locked tides it generates. Modern ocean forecasting systems, by assimilating the global constellation of nadir altimeters, already constrain the 4D mesoscale circulation—correctly positioning the eddies and stratification in space and time (*27*).

We test this hypothesis using one such data-assimilative forecast model (the HYbrid Coordinate Ocean Model, HYCOM (*28, 29*)). Crucially, this model does not assimilate SWOT data, making our validation against the satellite an independent test. We show that this physics-based simulation accurately reproduces not only the phase-locked internal tides but also, for the first time, a large fraction of the organized, fine-scale structure of the non-phase-locked variability. We demonstrate that this physics-based simulation can, for the first time, reproduce a large fraction of this non-phase-locked variability. This work provides a new pathway to correct satellite data and harness the full potential of high-resolution altimetry.

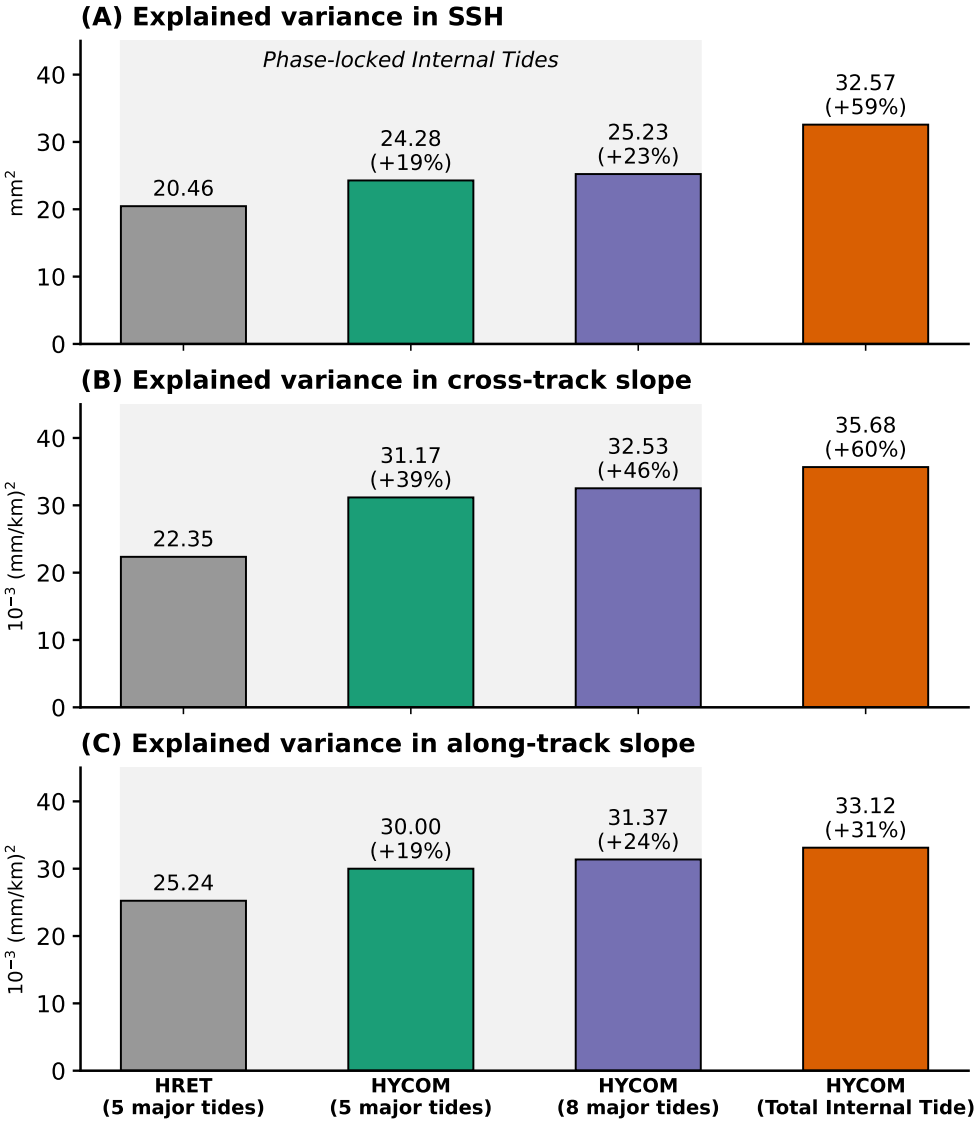

Figure 1: **HYCOM substantially improves explained variance of internal tides in SWOT.** Global mean explained variance for internal tide (**A**) sea surface height (SSH), (**B**) cross-track sea surface slope, and (**C**) along-track sea surface slopes, comparing SWOT observations to five model-derived products. The bars show the progressive improvement of HYCOM over the empirical HRET model. The comparison begins with an 'apples-to-apples' accounting of five phase-locked constituents, adds weaker constituents for the full phase-locked signal, and concludes with the total internal tide signal including its non-phase-locked component. Numerical values indicate the absolute explained variance, globally averaged across 584 SWOT passes, with the percent improvement over the HRET baseline shown in parentheses.

A New Benchmark for the Predictable Internal Tide

Before resolving the non-phase-locked tide, a model must first prove it can perform well for the predictable, phase-locked component. Our data-assimilative forecast model does so, substantially. Globally, our model explains 19% more SSH variance than the standard High Resolution Empirical Tide (HRET) atlas for the five principal constituents (Fig. 1A). This advantage grows to 23% when including weaker constituents (e.g., K_2, P_1, Q_1) that empirical atlases like HRET struggle to resolve from satellite data.

The model's superior performance is even more pronounced in the sea surface slopes—the fine-scale gradients critical for calculating geostrophic currents and high-resolution bathymetry (*30,31*). Our framework explains 39% more cross-track slope variance and 19% more along-track slope variance than HRET for the five major tides (Fig. 1B, C). These improvements climb to 46% and 24%, respectively, when the weaker tides are included, representing a significant advance for both physical oceanography and marine geology.

This enhanced performance is a near-global phenomenon, not an artifact of regional tuning. The model shows widespread improvements across all major ocean basins (Fig. 2). The skill is particularly strong over known internal tide generation "hotspots", such as the Hawaiian Ridge, the Luzon Strait, and the Mascarene Plateau. This correspondence between model improvement and known generation sites confirms the skill is rooted in an accurate representation of internal tide dynamics.

A constituent-by-constituent analysis reveals the sources of this performance (Fig. S1). The model's advantage is driven primarily by its high fidelity in simulating the semidiurnal tides (M_2, S_2, N_2), where it consistently outperforms HRET. (HRET does, however, show slightly better M_2 performance in some localized regions.) The picture is more nuanced for the diurnal tides. For both the O_1 and K_1 constituents, the empirical HRET model explains more variance than HYCOM across large areas of the Pacific. This suggests that regional inaccuracies in tidal forcing, bathymetry, or stratification, all critical for diurnal tide generation, may remain a challenge in the current simulation.

We also acknowledge that HRET's three-decade record averages over significant interannual climate variability (e.g., El Niño-Southern Oscillation, Indian Ocean Dipole) that can modulate

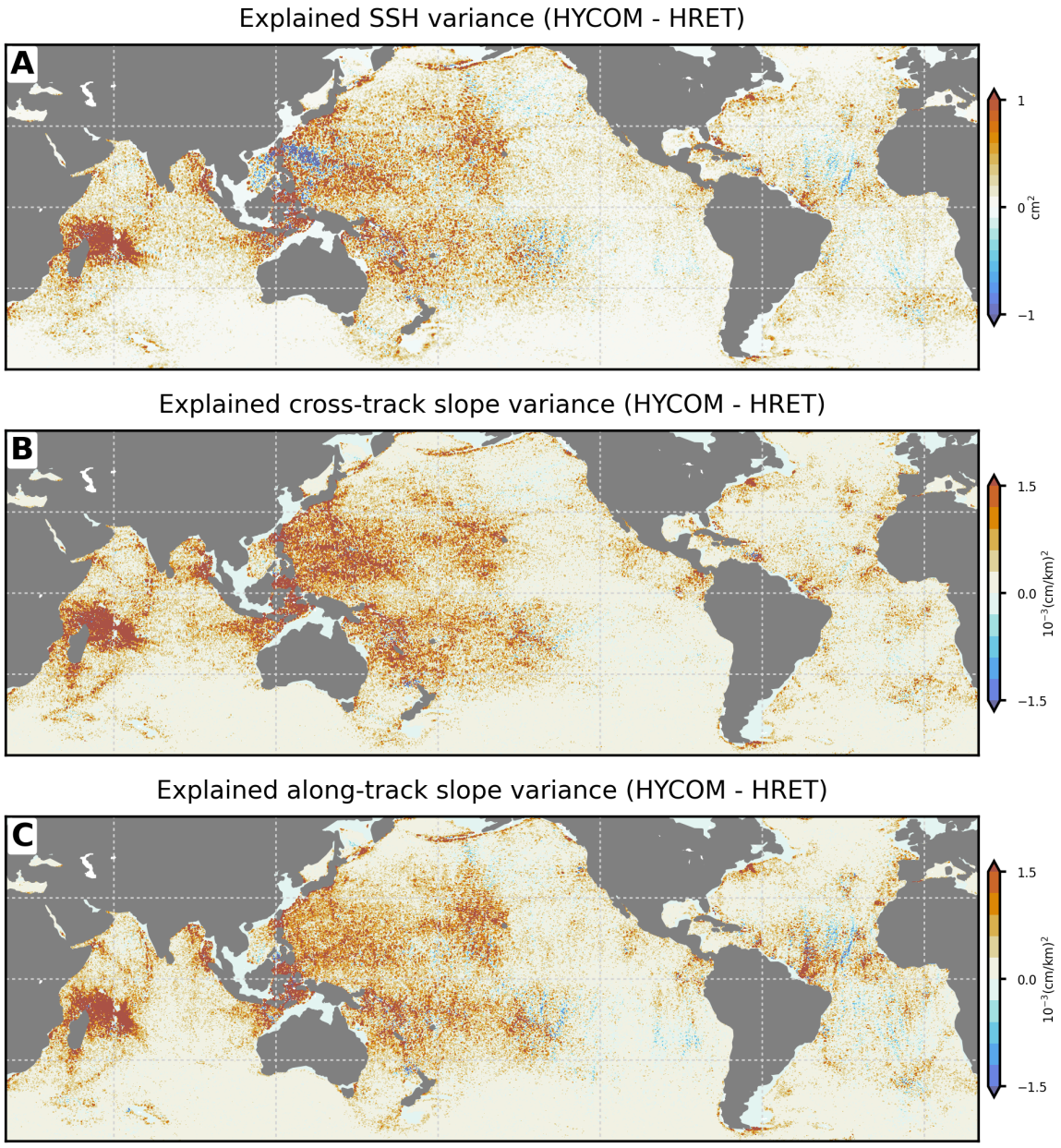

Figure 2: **HYCOM explains more phase-locked internal tide variance in SWOT SSH and slope than HRET.** (**A**) Difference in SSH variance in SWOT explained by HYCOM forecasts vs. HRET empirical model, based on five main tidal constituents contained in HRET. In red-shaded regions, HYCOM explains more variance than HRET, while HRET removes more variance in blue regions. (**B**) As in A, but for the variance of the cross-track sea surface slope. (**C**) As in A, but for the along-track sea surface slope.

internal tides (*32, 33*). In contrast, HYCOM's 18-month record, while sufficient for dominant tides, is more susceptible to aliasing non-phase-locked energy into its phase-locked component. Nevertheless, the sheer magnitude of the improvement, underpinned by the model's ability to resolve a richer vertical modal structure (*34, 35*), establishes a new benchmark. It suggests that data-assimilative models could be a useful complementary tool to empirical analysis for mapping the complex, phase-locked internal tide field, and may even provide superior performance in some respects.

Unmasking the Non-phase-locked Internal Tide

Our central finding is that the transient, non-phase-locked internal tide field is not random noise, but rather a predictable and spatially organized component of the global SSH (Figs. 3, S2, S3). This discovery is enabled by our model's high-frequency (hourly) output, which allows for robust tidal analysis over short timescales comparable to mesoscale decorrelation. Unlike traditional empirical analyses, which require long-term averaging that smooths out transient effects, our modeling approach captures the dynamic interaction between the tide field and the shifting mesoscale environment.

HYCOM explains a substantial fraction of this 'unpredictable' variability. Globally, this amounts to 10.32 mm^2 of total non-phase-locked explained variance (7.12 mm^2 semidiurnal and 2.98 mm^2 diurnal). This is not just a statistical fit; the model's own predicted non-phase-locked variance (9.11 mm^2) is realistic in magnitude and highly correlated with the observations. As shown in Figure 3, the model's predictive skill is highest nearby major topographic features, capturing large-scale propagation pathways radiating from hotspots like the Luzon Strait, Indonesian archipelago, and Madagascar.

This non-phase-locked variability is not a minor perturbation; it is often the dominant component of the total internal tide field (Figs. S4-S7). In vast areas of the open ocean, particularly in the far-field of generation sites, the non-phase-locked fraction exceeds 50% of the total internal tide energy, reaching over 70% in the semidiurnal band (Fig. S6). This pattern visually confirms the physical mechanism of decorrelation: as the internal tide propagates thousands of kilometers, it continuously interacts with the turbulent mesoscale eddy field, which scatters its energy and breaks its phase

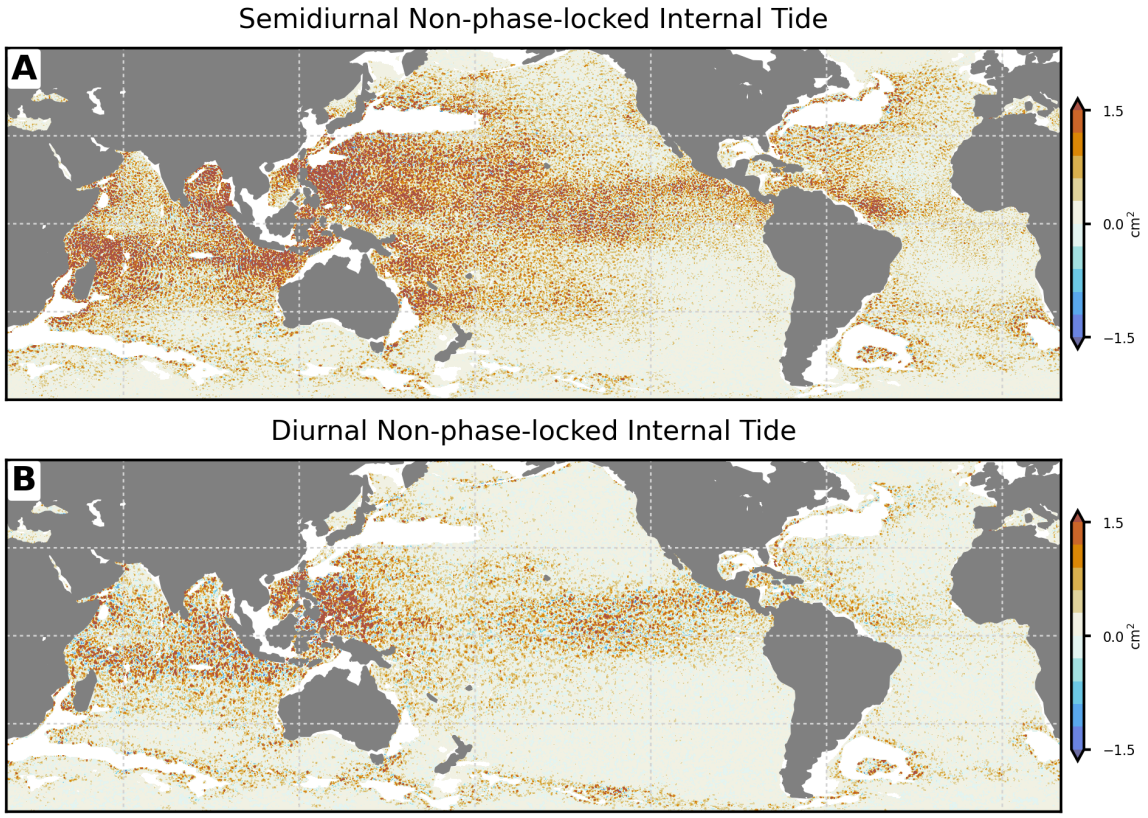

Figure 3: **Assessment of HYCOM's skill in representing non-phase-locked internal tides.** Explained variance of SSH from non-phase-locked internal tides in the (**A**) semidiurnal and (**B**) diurnal frequency bands, comparing HYCOM simulations to SWOT satellite altimetry. High explained variance (red) indicates where the model successfully captures incoherent tide signals, particularly nearby major generation sites and along their propagation pathways. Negative values (blue) denote regions where the model's predicted changes are opposite to those observed.

relationship with the astronomical forcing. The absolute variance of this signal is largest in the climatically critical Indo-Pacific warm pool, where non-phase-locked internal tides represent a major reservoir of ocean energy (Fig. S5).

To determine if this incoherence persists in the most energetic regimes, we analyzed the non-phase-locked fraction as a function of the total internal tide variance (Fig. S6, S7). This analysis shows that non-phase-locked variability is a fundamental feature of the internal tide field at all energy levels, highlighting that incoherence is a significant component even in major internal tide generation hotspots. Even when restricting the analysis to only the most energetic locations (those in the top few percentiles of internal tide variance) the non-phase-locked component still accounts for a substantial portion of the signal. At the highest energy thresholds, the incoherent fraction remains at approximately 39% for the semidiurnal band and 14% for the diurnal band. This persistence establishes incoherence as a pervasive and fundamental aspect of internal tide dynamics.

These results are broadly consistent with, and extend, prior global estimates for semidiurnal tides. Previous studies using nadir altimetric wavenumber spectra suggest that roughly 44% of global semidiurnal internal tide variance is incoherent (*36*). Comparable simulations using coarser, non-data-assimilative HYCOM yields fractions ranging from 41% to 49% (*37, 38*), and Argo float measurements at 1000 dbar indicate even higher incoherent fractions, reaching up to 85% in the deep ocean (*24*).

Despite this advance, certain dynamically complex regions remain challenging. Regional patterns of model-data disagreement are present in areas such as the northern Pacific and the central Atlantic (Figs. 3, S2, S3). These discrepancies, which may result from localized inaccuracies in bathymetry or model physics (*34*), highlight priority areas for future model development.

Lifting the Internal Tide Veil

By modeling both its phase-locked and non-phase-locked components, our framework provides a comprehensive, physically consistent representation of the total internal tide field. This establishes a new benchmark for satellite altimetry correction. Globally, HYCOM explains a total of 32.57 mm^2 of variance in SWOT SSH observations, a 59% improvement over the HRET atlas (Fig. 1A). This advantage extends to the sea surface slopes, where our framework explains 60% more variance in

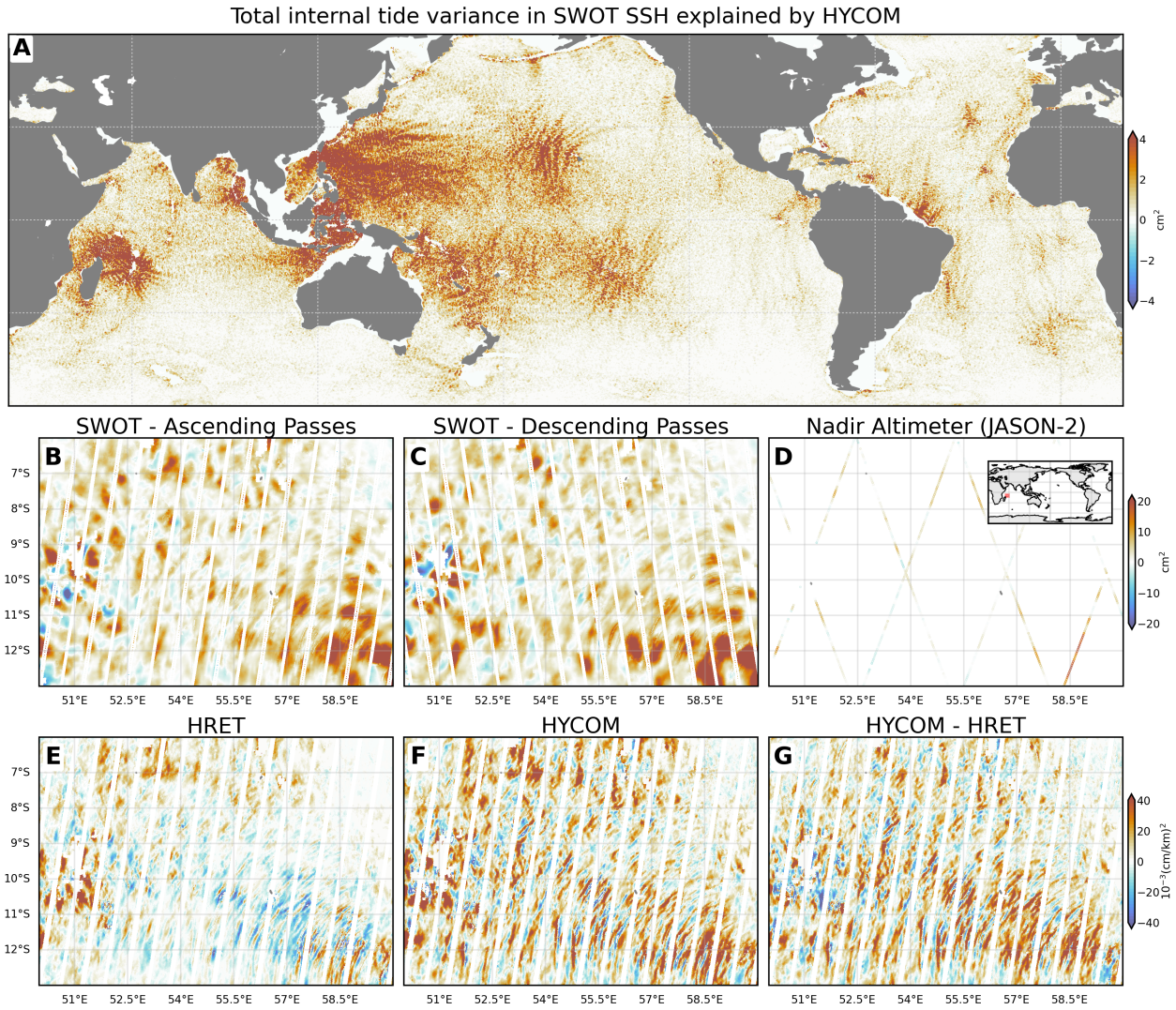

Figure 4: **HYCOM resolves total internal tide variance in SWOT observations.** (**A**) Global map of SSH variance explained by HYCOM's total (phase-locked and non-phase-locked) internal tide signal. (**B** to **D**) Regional zoom over the Indian Ocean comparing explained SSH variance for SWOT's ascending (**B**) and descending (**C**) passes with that from the nadir altimeter JASON-2 (**D**), highlighting the resolution gain from wide-swath data. (**E** to **G**) Comparison of explained cross-track slope variance for the empirical HRET model (**E**), HYCOM (**F**), and the improvement by HYCOM (HYCOM - HRET) (**G**). In (**A**–**F**), positive values (red) indicate model skill. In (**G**), red highlights regions where HYCOM outperforms HRET. These results demonstrate a substantial advance in resolving internal tide signals by high-resolution, physics-based data-assimilative modeling validated against next-generation wide-swath altimetry.

the cross-track slope and 31% more in the along-track slope (Fig. 1B, C). The resulting global map reveals the full extent of the internal tide's influence, showing interconnected corridors of energy stretching across entire ocean basins (Fig. 4A, S8).

This observational leap is driven by the synergy between high-resolution data-assimilative modeling and SWOT's wide-swath technology. Traditional nadir altimeters provided only sparse, one-dimensional traces (Fig. 4D), while SWOT resolves the full two-dimensional structure of these wave fields (Fig. 4B, C). Our model's ability to capture the distinct variance patterns seen by SWOT on both ascending and descending satellite passes validates that we are resolving the directional, small-scale signatures of internal tide propagation. This capability also extends to the sea surface slopes (Fig. 4E-G; S8), which are essential for deriving accurate ocean currents and bathymetry from SWOT.

A primary challenge in this analysis is the potential for energy from the mesoscale eddy field to 'leak' into our non-phase-locked estimates, as both can exhibit variability in overlapping frequency bands. We addressed this potential contamination in two ways. First, we mitigated the most significant impacts by masking regions of high eddy variance from our statistics (Fig. 1). Second, we quantified the remaining non-tidal 'noise floor' by computing the explained variance in the adjacent sub-tidal and super-tidal frequency bands.

The average explained variance in these non-tidal bands is approximately 1.96 mm^2 (Fig. S9), which accounts for only 6% of the total explained tidal variance (32.57 mm^2). While the resulting maps already show clear, large-scale tidal propagation pathways distinct from typical mesoscale structures (Fig. 3), the large separation between the in-band signal and out-of-band noise gives high confidence that our framework is resolving physical tidal processes. The precise quantification of any remaining leakage remains a priority for future work, but these findings represent a first-order, physically consistent validation.

The ability of this simulation to account for such a large fraction of the total observed variability validates its physical realism. We note that this total explained variance is not a simple linear sum of the individual components. A perfect separation of variance is challenging due to non-orthogonalities inherent in the harmonic analysis of a time-varying field. This, however, does not detract from the model's overall predictive power. This work provides a physically consistent, validated tool to correct for the energetic internal tide field, a necessary step for accurately observing

the global submesoscale ocean circulation.

Conclusions

By resolving the deterministic structure of the full internal tide field, this work lowers a barrier to observing Earth's climate system from space. The observational challenge of the SWOT mission, whereby its high-resolution measurements were obscured by tidal noise, is now largely addressed. Our validation against SWOT's measurements revises the view of an unpredictable tidal background, demonstrating that the non-phase-locked component is a globally structured and quantifiable field. By re-characterizing this source of observational error as a predictable feature, we provide the tool required to lift the tidal veil from satellite records.

This has immediate implications. We have demonstrated the capability to separate the energetic signature of the total internal tide field from the fine-scale circulation it obscures. This capability yields a clearer view of the mesoscale and submesoscale eddies that form the ocean's climate engine. This also provides the sea surface slope data required for improvements in mapping seafloor bathymetry (*31*). In doing so, our work advances the scientific utility of the SWOT mission (*39*) and is a step in our ability to observe and understand the physical processes that govern Earth's climate.

This result moves beyond mere correction and toward new scientific frontiers. The predictability of the non-phase-locked field enables, for example, targeted studies of its direct impact on biogeochemical cycles and underwater acoustic propagation (*40*). However, this work also highlights the next major challenge: accounting for the entire internal wave continuum. While this study resolves the deterministic, high-energy tidal peaks, these exist within a broad spectrum, much of which is stochastic and more difficult to simulate. By deterministically resolving the most powerful component of this field, our work provides the essential baseline required to guide these future efforts.

The path forward will involve tackling remaining challenges, such as refining models in eddy-rich regions and improving fine-scale bathymetric data. A promising approach is a new generation of non-hydrostatic models (*41*), embedded as high-resolution regional simulations using global models like HYCOM for their boundary conditions (*42*), allowing for the dynamic downscaling

of the oceanic energy cascade (*43*). This framework, combined with the next generation of *in-situ* platforms, will be essential for creating a full four-dimensional view of the oceanic energy cascade. Achieving this will allow us to understand not only the ocean's hidden dynamics today but also how this energetic landscape will evolve on our changing planet.

References and Notes

1. B. D. Hamlington, J. K. Willis, N. Vinogradova, The Emerging Golden Age of Satellite Altimetry to Prepare Humanity for Rising Seas. *Earth's Future* **11** (11) (2023), doi:10.1029/2023ef003673.

2. A. Mahadevan, The Impact of Submesoscale Physics on Primary Productivity of Plankton. *Annual Review of Marine Science* **8** (1), 1–24 (2014), doi:10.1146/annurev-marine-010814-015912.

3. C. Wunsch, Internal tides in the ocean. *Reviews of Geophysics* **13** (1), 167–182 (1975).

4. M. C. Buijsman, B. K. Arbic, S. M. Kelly, A. F. Waterhouse, Internal Gravity Waves, Encyclopedia of Ocean Sciences, pp. 622–632 (2019), doi:10.1016/b978-0-12-409548-9.04160-9.

5. R. D. Ray, G. T. Mitchum, Surface manifestation of internal tides generated near Hawaii. *Geophysical Research Letters* **23** (16), 2101–2104 (1996).

6. B. D. Dushaw, B. M. Howe, B. D. Cornuelle, P. F. Worcester, D. S. Luther, Barotropic and baroclinic tides in the central North Pacific Ocean determined from long-range reciprocal acoustic transmissions. *Journal of Physical Oceanography* **25** (4), 631–647 (1995).

7. E. Kunze, Internal-Wave-Driven Mixing: Global Geography and Budgets. *Journal of Physical Oceanography* **47** (6), 1325–1345 (2017), 1520-0485, doi:10.1175/jpo-d-16-0141.1.

8. J. A. MacKinnon, *et al.*, Climate Process Team on Internal Wave-Driven Ocean Mixing. *Bull Am Meteorol Soc* **98** (11), 2429–2454 (2017), doi:10.1175/bams-d-16-0030.1.

9. C. Vic, *et al.*, Deep-ocean mixing driven by small-scale internal tides. *Nat Commun* **10** (1), 2099 (2019), doi:10.1038/s41467-019-10149-5.

10. C. B. Whalen, *et al.*, Internal wave-driven mixing: governing processes and consequences for climate. *Nature Reviews Earth & Environment* **1** (11), 606–621 (2020), doi:10.1038/s43017-020-0097-z.

11. S. Abdalla, *et al.*, Altimetry for the future: Building on 25 years of progress. *Advances in Space Research* **68** (2), 319–363 (2021), doi:10.1016/j.asr.2021.01.022.

12. D. Stammer, A. Cazenave, *Satellite altimetry over oceans and land surfaces* (CRC press) (2017).

13. R. Morrow, *et al.*, Global Observations of Fine-Scale Ocean Surface Topography With the Surface Water and Ocean Topography (SWOT) Mission. *Frontiers in Marine Science* **6** (2019), doi:10.3389/fmars.2019.00232.

14. L. Fu, *et al.*, The Surface Water and Ocean Topography Mission: A Breakthrough in Radar Remote Sensing of the Ocean and Land Surface Water. *Geophysical Research Letters* **51** (4) (2024), doi:10.1029/2023gl107652.

15. M. Archer, J. Wang, P. Klein, G. Dibarboure, L.-L. Fu, Wide-swath satellite altimetry unveils global submesoscale ocean dynamics. *Nature* **640** (8059), 691–696 (2025), doi:10.1038/s41586-025-08722-8.

16. J. Wang, *et al.*, SWOT Mission Validation of Sea Surface Height Measurements at Sub-100 km Scales. *Geophysical Research Letters* **52** (11) (2025), doi:10.1029/2025gl114936.

17. G. T. Mitchum, S. M. Chiswell, Coherence of internal tide modulations along the Hawaiian Ridge. *Journal of Geophysical Research: Oceans* **105** (C12), 28653–28661 (2000), doi:10.1029/2000jc900140.

18. B. Dushaw, An empirical model for mode-1 internal tides derived from satellite altimetry: Computing accurate tidal predictions at arbitrary points over the world oceans. *University of Washington Applied Physics Laboratory Tech. Rep* (2015).

19. E. D. Zaron, Baroclinic Tidal Sea Level from Exact-Repeat Mission Altimetry. *Journal of Physical Oceanography* **49** (1), 193–210 (2019), 1520-0485, doi:10.1175/jpo-d-18-0127.1.

20. L. Carrère, *et al.*, Accuracy assessment of global internal-tide models using satellite altimetry. *Ocean Science* **17** (1), 147–180 (2021), doi:10.5194/os-17-147-2021.

21. Z. Zhao, A new-generation internal tide model based on 30 years of satellite sea surface height measurements: multiwave decomposition and isolated beams. *Earth System Science Data* **17** (8), 3949–3974 (2025), doi:10.5194/essd-17-3949-2025.

22. H. v. Haren, Incoherent internal tidal currents in the deep ocean. *Ocean Dynamics* **54** (1), 66–76 (2004), 1616-7228, doi:10.1007/s10236-003-0083-2.

23. R. D. Ray, E. D. Zaron, Non-stationary internal tides observed with satellite altimetry. *Geophysical Research Letters* **38** (17), n/a–n/a (2011), doi:10.1029/2011gl048617.

24. G. Geoffroy, J. Nycander, Global Mapping of the Nonstationary Semidiurnal Internal Tide Using Argo Data. *Journal of Geophysical Research: Oceans* **127** (4) (2022), doi:10.1029/2021jc018283.

25. B. Yadidya, *et al.*, Phase-Accurate Internal Tides in a Global Ocean Forecast Model: Potential Applications for Nadir and Wide-Swath Altimetry. *Geophysical Research Letters* **51** (4) (2024), doi:10.1029/2023gl107232.

26. B. Yadidya, *et al.*, Predicting internal tides with a global ocean forecast system: Insights from SWOT CalVal orbit (2025), doi:10.22541/essoar.174164232.20506498/v1.

27. P.-Y. L. Traon, *et al.*, Satellite altimetry and operational oceanography: from Jason-1 to SWOT. *Ocean Science* **21** (4), 1329–1347 (2025), doi:10.5194/os-21-1329-2025.

28. E. Chassignet, *et al.*, US GODAE: Global Ocean Prediction with the HYbrid Coordinate Ocean Model (HYCOM). *Oceanography* **22** (2), 64–75 (2009), doi:10.5670/oceanog.2009.39.

29. E. J. METZGER, *et al.*, US Navy Operational Global Ocean and Arctic Ice Prediction Systems. *Oceanography* **27** (3), 32 (2014).

30. Y. Yu, D. T. Sandwell, G. Dibarboure, C. Chen, J. Wang, Accuracy and Resolution of SWOT Altimetry: Foundation Seamounts. *Earth and Space Science* **11** (6) (2024), doi:10.1029/2024ea003581.

31. Y. Yu, D. T. Sandwell, G. Dibarboure, Abyssal marine tectonics from the SWOT mission. *Science* **386** (6727), 1251–1256 (2024), doi:10.1126/science.ads4472.

32. M. Tchilibou, *et al.*, Internal tides in the Solomon Sea in contrasted ENSO conditions. *Ocean Science* **16** (3), 615–635 (2020), doi:10.5194/os-16-615-2020.

33. B. Yadidya, A. D. Rao, Interannual variability of internal tides in the Andaman Sea: an effect of Indian Ocean Dipole. *Sci Rep* **12** (1), 11104 (2022), doi:10.1038/s41598-022-15301-8.

34. M. C. Buijsman, *et al.*, On the interplay between horizontal resolution and wave drag and their effect on tidal baroclinic mode waves in realistic global ocean simulations. *Ocean Modelling* **152** (2020), doi:10.1016/j.ocemod.2020.101656.

35. M. C. Buijsman, *et al.*, Energetics of (Super)Tidal Baroclinic Modes in a Realistically Forced Global Ocean Simulation. *Journal of Geophysical Research: Oceans* **130** (6) (2025), doi: 10.1029/2025jc022460.

36. E. D. Zaron, Mapping the nonstationary internal tide with satellite altimetry. *Journal of Geophysical Research: Oceans* **122** (1), 539–554 (2017), 2169-9291, doi:10.1002/2016jc012487.

37. A. C. Savage, *et al.*, Frequency content of sea surface height variability from internal gravity waves to mesoscale eddies. *Journal of Geophysical Research: Oceans* **122** (3), 2519–2538 (2017), 2169-9291, doi:10.1002/2016jc012331.

38. A. D. Nelson, *et al.*, Toward Realistic Nonstationarity of Semidiurnal Baroclinic Tides in a Hydrodynamic Model. *Journal of Geophysical Research: Oceans* **124** (9), 6632–6642 (2019), doi:10.1029/2018jc014737.

39. G. Dibarboure, *et al.*, Blending 2D topography images from the Surface Water and Ocean Topography (SWOT) mission into the altimeter constellation with the Level-3 multi-mission Data Unification and Altimeter Combination System (DUACS). *Ocean Sci.* **21** (1), 283–323 (2025), OS Altimetry, SWOT, doi:10.5194/os-21-283-2025.

40. M. C. Schönau, *et al.*, HOW DO TIDES AFFECT UNDERWATER ACOUSTIC PROPAGATION? *Oceanography* (38(2)) (2025), doi:10.5670/oceanog.2025.308.

41. F. Auclair, *et al.*, A non-hydrostatic non-Boussinesq algorithm for free-surface ocean modelling. *Ocean Modelling* **132**, 12–29 (2018), doi:10.1016/j.ocemod.2018.07.011.

42. M. S. Solano, *et al.*, Nonlinear internal tides in a realistically forced global ocean simulation. *Journal of Geophysical Research: Oceans* **128** (12), e2023JC019913 (2023).

43. J. Skitka, *et al.*, Internal-Wave Dissipation Mechanisms and Vertical Structure in a High-Resolution Regional Ocean Model. *Geophysical Research Letters* **51** (17) (2024), doi:10.1029/2023gl108039.

44. AVISO/DUACS, The SWOT L3_LR_SSH product, derived from the L2 SWOT KaRIn low rate ocean data products (NASA/JPL and CNES), is produced and made freely available by AVISO and DUACS teams as part of the DESMOS Science Team project (2024), SWOT Level-3 KaRIn Low Rate SSH Expert (v2.0.1).

45. A. Tréboutte, *et al.*, KaRIn Noise Reduction Using a Convolutional Neural Network for the SWOT Ocean Products. *Remote Sensing* **15** (8), 2183 (2023), doi:10.3390/rs15082183.

46. M. Tchilibou, *et al.*, Internal tides off the Amazon shelf in the western tropical Atlantic: analysis of SWOT Cal/Val mission data. *Ocean Sci.* **21** (1), 325–342 (2025), OS, doi:10.5194/os-21-325-2025.

47. E. D. Zaron, S. Elipot, Estimates of Baroclinic Tidal Sea Level and Currents from Lagrangian Drifters and Satellite Altimetry. *Journal of Atmospheric and Oceanic Technology* **41** (8), 781–802 (2024), doi:10.1175/jtech-d-23-0159.1.

48. R. Bleck, An oceanic general circulation model framed in hybrid isopycnic-Cartesian coordinates. *Ocean modelling* **4** (1), 55–88 (2002).

49. E. P. Chassignet, *et al.*, Ocean prediction with the hybrid coordinate ocean model (HYCOM), in *Ocean weather forecasting: an integrated view of oceanography* (Springer), pp. 413–426 (2006).

50. J. A. Cummings, O. M. Smedstad, Variational data assimilation for the global ocean, Data assimilation for atmospheric, oceanic and hydrologic applications (Vol. II) (Springer), pp. 303–343 (2013).

51. S. R. Jayne, L. C. S. Laurent, Parameterizing tidal dissipation over rough topography. *Geophysical Research Letters* **28** (5), 811–814 (2001), 1944-8007, doi:10.1029/2000gl012044.

52. H. E. Ngodock, *et al.*, On improving the accuracy of the M2 barotropic tides embedded in a high-resolution global ocean circulation model. *Ocean Modelling* **97**, 16–26 (2016), doi:10.1016/j.ocemod.2015.10.011.

53. T. Hogan, *et al.*, The Navy Global Environmental Model. *Oceanography* **27** (3), 116–125 (2014), doi:10.5670/oceanog.2014.73.

54. M. C. Buijsman, *et al.*, Semidiurnal internal tide incoherence in the equatorial Pacific. *Journal of Geophysical Research: Oceans* **122** (7), 5286–5305 (2017), 2169-9291, doi:10.1002/2016jc012590.

Acknowledgments

BKA is grateful for sabbatical support from the Australian National University, especially Callum Shakespeare, Andy Hogg, and Adele Morrison, during the 2024–2025 academic year. This research made use of computational resources provided by Advanced Research Computing at the University of Michigan, a computer time grant from the Department of Defense (DoD) High Performance Computing Modernization Program at the Navy DoD Supercomputing Resource Center, computing resources from the NASA Advanced Supercomputing (NAS) Division at Ames Research Center, and storage from the OSiRIS project at the University of Michigan. This is NRL contribution NRL/JA/7320-25-6995 and is approved for public release.

Funding: BY, BKA, EPC, JFS, and MCB acknowledge support from the Office of Naval Research (ONR) through grants N00017-22-1-2576 (BY, BKA, MCB), N001422-1-2574 (EPC), and 02507017106655 (JFS), as part of the Global Internal Waves project under the National Oceanographic Partnership Program (`https://nopp-giw.ucsd.edu/`). Additional support for BKA, EPC, JFS, and MCB was provided by NASA grants 80NSSC20K1135 and 80NSSC24K1649. EDZ was supported by NASA grants 80NSSC21K1189 and 80NSSC24K1645.

Author contributions: Conceptualization: B.Y., B.K.A., J.F.S., E.D.Z., M.C.B. Methodology: B.Y., B.K.A, J.F.S., E.D.Z., M.C.B., L.C., M.T. Formal analysis and investigation: B.Y. Data curation: B.Y., J.F.S. Writing – original draft: B.Y. Writing – review and editing: B. Y., B.K.A, J.F.S., E.D.Z., M.C.B., E.P.C., L.C., M.T. Visualization: B.Y. Project administration and financing acquisition: B.K.A., J.F.S., M.C.B., E.P.C.

Competing interests: There are no competing interests to declare.

Data and materials availability: The Level 3 SWOT ocean products used in this study are publicly available and were obtained from the CNES/Aviso+ altimetry data portal (*44*). The specific product information can be found at: `https://www.aviso.altimetry.fr/en/data/products/sea-surface-height-products/global/swot-l3-ocean-products.html`. The Python code necessary for reproducing the figures and applying the HYCOM-based internal tide corrections will be made publicly available through a repository upon the acceptance of this manuscript for publication.

Supplementary materials

Materials and Methods

Figs. S1 to S8

References *(45-54)*

Supplementary Materials for

Resolving Global Internal Tides Reveals Fine-Scale Ocean Circulation

Badarvada Yadidya*, Brian K. Arbic, Jay F. Shriver, Edward D. Zaron,
Maarten C. Buijsman, Eric P. Chassignet, Loren Carrère, Michel Tchilibou
*Corresponding author. Email: yadidyabadarvada@gmail.com

This PDF file includes:

Materials and Methods

Figures S1 to S8

Materials and Methods

SWOT Satellite Sea Surface Height Observations

We use the SWOT Level-3 KaRIn low-rate SSH dataset (alpha v2.0.1), available via the AVISO repository (`https://doi.org/10.24400/527896/A01-2023.018`). Our primary dataset is the `ssha_filtered` variable (*45*), which incorporates geophysical corrections including barotropic and baroclinic tides, dynamic atmosphere, wet-troposphere delays, sea-state biases, and time-mean dynamic topography; we subsequently add back the HRET internal tide correction to get the full internal tide signal in the SSH. Furthermore, we removed large-scale ocean signals, including mesoscale eddies by applying the `duacs_ssha_karin_2_oi` product (*26, 46*).

Following completion of the calibration and validation (Cal/Val) fast-sampling phase (1-day repeat orbit, March–July 2023), SWOT transitioned on 21 July 2023 to its nominal 21-day repeat orbit (science phase). On this science orbit, SWOT completes 292 unique orbits per cycle over ~21 days, providing near-global coverage between 78°S and 78°N.

During the 21-day repeat cycle, Ka-band Radar Interferometer (KaRIn) acquires SSH across two ~60 km swaths on either side of nadir (total ~120 km swath width), with a ~20 km nadir gap and along- and across-track sampling at ~2 km resolution. The revisit frequency varies by latitude—2 repeats per cycle at the equator, rising to ≥6 at high latitudes.

This science-orbit configuration trades reduced temporal revisit (compared to the 1-day Cal/Val phase) for substantially improved spatial sampling and near-global coverage, enabling comprehensive observation of mesoscale and submesoscale ocean structure during the science phase. Analyses in this paper focus exclusively on data from the 21-day science orbit, covering July 2023 to December 2024 and spanning the first 25 cycles.

Empirical Internal Tide Atlas: HRET

The HRET22 internal tide atlas (merger of versions 8.1 and 14) provides a global, empirically derived estimate of phase-locked internal tide signals based on nearly all available exact-repeat nadir altimeter data spanning 1992 to 2021 (*19, 47*). The dataset incorporates observations from TOPEX/Poseidon, Jason-1/2/3, GEOSAT, ERS-1/2, and Envisat missions.

HRET provides mode-1 and mode-2 internal tide estimates at five major tidal frequencies—M_2,

S_2, N_2, K_1, and O_1—on a uniform $0.05° \times 0.05°$ (1/20°) global grid. The final product includes a quality control mask that excludes regions where signal extraction is unreliable due to low signal-to-noise ratio or aliasing effects, effectively identifying areas where internal tide amplitudes are deemed excessively noisy or inconsistent.

HYCOM Forecast Ocean Model Simulations

We use a global, data-assimilative configuration of the Hybrid Coordinate Ocean Model (HYCOM) spanning July 2023 to December 2024. This simulation was executed in two consecutive phases: EXPT 22.3 (July 2023–August 2024) and EXPT 3.1 (September–December 2024), both sharing identical model setups and data assimilation systems. The model is run on a $1/25°$ tri-polar grid with nominal horizontal resolution of approximately 3 km at mid-latitudes and 41 hybrid vertical layers. The vertical coordinate system transitions smoothly between z-level (depth-based), isopycnal (density-based), and sigma (terrain-following) coordinates, adapting dynamically to local oceanographic conditions (*48, 49*).

Data assimilation is conducted using the Navy Coupled Ocean Data Assimilation (NCODA) system (*50*), a three-dimensional variational (3DVAR) scheme with a 24-hour assimilation window and 3-hour Incremental Analysis Updates. All active nadir altimeter data are assimilated via synthetic profiles to map the geostrophic flow, with the important exception of SWOT, which is not included in the data assimilation process. Assimilated observations thus include de-tided measurements from all other operating nadir altimeters, satellite and *in-situ* sea surface temperature, and temperature and salinity profiles from Argo floats, moored buoys, and expendable bathythermographs (XBTs). Daily mean fields are filtered to exclude tidal variability, enabling improved representation of mesoscale and seasonal ocean dynamics. Because SWOT data are not assimilated, our comparison with SWOT SSH provides an independent assessment: the model has no access to the high-resolution mesocale information uniquely observed by SWOT.

Astronomical tidal forcing is applied using eight major constituents: M_2, S_2, N_2, K_2, K_1, O_1, P_1, and Q_1. Barotropic tide accuracy is enhanced through two mechanisms: a topographic wave drag parameterization (*51*) that accounts for unresolved internal wave generation over steep topography, and an Augmented State Ensemble Kalman Filter (ASEnKF) that assimilates altimetric observations to refine the barotropic tidal signal (*52*).

Surface atmospheric forcing is provided by the Navy Global Environmental Model (NAVGEM) (*53*), which offers fields at 0.17° resolution with 60 vertical levels extending up to 19 km altitude. Subgrid-scale vertical mixing is handled using the K-profile parameterization (KPP) scheme.

To isolate internal tide signals from the model SSH output, we first regrid the native 1/25° HYCOM hourly fields onto a uniform 4 km grid and then apply two-dimensional Gaussian spatial filters to suppress large-scale and barotropic variability. A 300 km cutoff is used to extract semidiurnal signals, while a 500 km cutoff isolates diurnal variability (*25*). To minimize leakage from coastal effects and large-scale barotropic tides, we mask out grid cells shallower than 1,000 m (semidiurnal) and 1,500 m (diurnal). Throughout this study, we define the *filtered SSH* as the residual obtained by subtracting the Gaussian-smoothed SSH field from the total HYCOM SSH. This filtered SSH isolates internal tide variability and is used as the primary representation of the internal tide signal. The combined 18-month dataset from EXPT 22.3 and EXPT 3.1 fully overlaps with the first 25 cycles of SWOT's 21-day science orbit, providing a consistent and high-resolution model baseline for internal tide evaluation.

Estimation of Phase-Locked and Non-Phase-Locked Internal Tides

To quantify both the phase-locked and non-phase-locked internal tide signals, we first carried out all computations on a uniform 4 km grid using *filtered SSH* from HYCOM. The phase-locked internal tide signal, denoted η_{pl}, was extracted via harmonic tidal analysis applied to the *filtered SSH* time series at each grid point. This analysis was performed for eight principal tidal constituents: M_2, S_2, N_2, K_2, K_1, O_1, P_1, and Q_1. The resulting decomposition yielded the harmonic constants—amplitude A_n, frequency ω_n, and phase ϕ_n—at each location on the grid, representing the deterministic, phase-locked component of the internal tide field.

Simultaneously, we isolated internal tide variability within the diurnal and semidiurnal frequency bands by applying a fourth-order Butterworth bandpass filter (*54*) to the same SSH dataset. The filter retained spectral energy between 0.8–1.2 cycles per day (cpd) for the diurnal band and 1.8–2.2 cpd for the semidiurnal band. The bandpass-filtered SSH, denoted $\tilde{\eta}_{\mathrm{BP}}(t)$, is defined as:

$$\tilde{\eta}_{\mathrm{BP}}(t) = h(t) * \eta(t), \tag{S1}$$

where $h(t)$ represents the Butterworth transfer function and $*$ denotes convolution in the time

domain.

The phase-locked IT signal $\tilde{\eta}_{\mathrm{pl}}(t)$ was then reconstructed on the 4 km grid using the standard tidal synthesis equation:

$$\tilde{\eta}_{\mathrm{pl}}(t) = \sum_{n} A_n \cos\left(\omega_n t + \phi_n\right), \tag{S2}$$

where the summation index n runs over the eight tidal constituents listed above.

The residual non-phase-locked internal tide signal, $\tilde{\eta}_{\mathrm{npl}}(t)$, was computed by subtracting the phase-locked reconstruction from the bandpass-filtered SSH:

$$\tilde{\eta}_{\mathrm{npl}}(t) = \tilde{\eta}_{\mathrm{BP}}(t) - \tilde{\eta}_{\mathrm{pl}}(t). \tag{S3}$$

Once computed, both the phase-locked and non-phase-locked IT signals were regridded from the 4 km HYCOM grid onto SWOT's 21-day ground track coordinates using a nearest-neighbor search based on a k-dimensional tree (KD-tree) algorithm. This approach efficiently identifies the closest model grid point to each SWOT track location in space, ensuring spatial alignment between the modeled internal tide fields and the SWOT sampling geometry.

A known challenge of bandpass filtering is the potential for leakage from mesoscale eddies, whose energy can leak into the internal tide frequency bands, particularly in dynamically active regions. To directly address this issue, we completely mask out the regions with strong eddies in our non-phase-locked internal tide signal. These regions are defined as any location where the AVISO-derived sea level variance exceeds 200 cm^2. While this approach targets the most significant leakage, our final $\tilde{\eta}_{\mathrm{npl}}$ estimates are likely not entirely free of residual eddy signals.

Sea Surface Slope

To assess model performance in representing the horizontal structure of internal tides, we computed sea surface slope components from the SSH fields. Slopes were calculated for both SWOT observations and model outputs on the 2-km SWOT ground track using a first-order, centered finite difference scheme. The local grid spacings, dx (cross-track) and dy (along-track), were calculated at each point using the Haversine formula to account for Earth's curvature. This process yielded two orthogonal slope components: the cross-track slope (∇_xSSH) and the along-track slope (∇_ySSH), both defined on an interior grid.

Explained Variance Statistics

We quantify model performance for both SSH and it's slope using 'explained variance' (often referred to as *variance reduction*), defined as the variance in the SWOT signal that is captured by a given model. This approach follows previously established methodologies (*19, 20, 25, 26*). The explained variance is computed as:

$$\text{Explained variance} = \text{Var}(\text{Signal}_{\text{SWOT}}) - \text{Var}(\text{Signal}_{\text{SWOT}} - \text{Signal}_{\text{Model}}), \tag{S4}$$

where Var denotes the temporal variance at a given spatial location. The term Signal represents the variable of interest and their phase-locked and non-phase-locked components, which include the total SSH time series, the cross-track slope (∇_xSSH), and the along-track slope (∇_ySSH). To ensure a valid calculation when isolating the non-phase-locked component, the phase-locked signal is removed from the $\text{Signal}_{\text{SWOT}}$ prior to computing the explained variance statistics. A higher explained variance in any of these metrics indicates a better match between the model and observations, and is therefore indicative of superior model skill. This same statistic is also computed and averaged for the non-tidal frequency bands (1.4-1.8 cpd and 2.2-2.6 cpd) to provide a rough estimate of the noise floor in the semidiurnal tidal band.

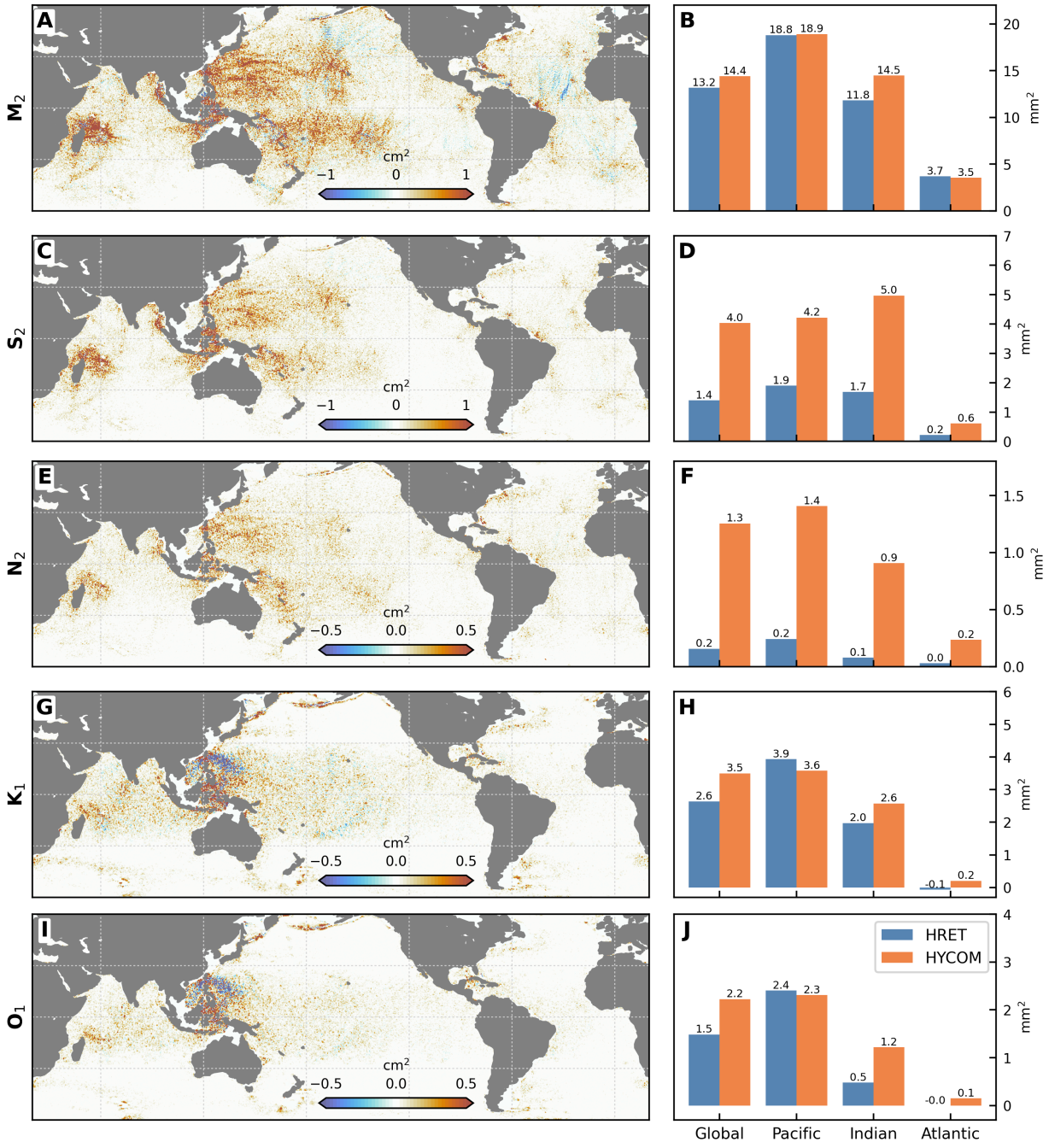

Figure S1: **Difference between HYCOM and HRET in explaining phase-locked internal tide variance in SWOT SSH for major tides.** (**A**, **C**, **E**, **G**, **I**) Maps for individual tidal constituents (M_2, S_2, N_2, K_1, O_1) further resolve model skill differences by frequency. (**B**, **D**, **F**, **H**, **J**) Adjacent bar plots summarize the mean explained variance for each ocean basin and for the aggregate signal, comparing HYCOM and HRET performance.

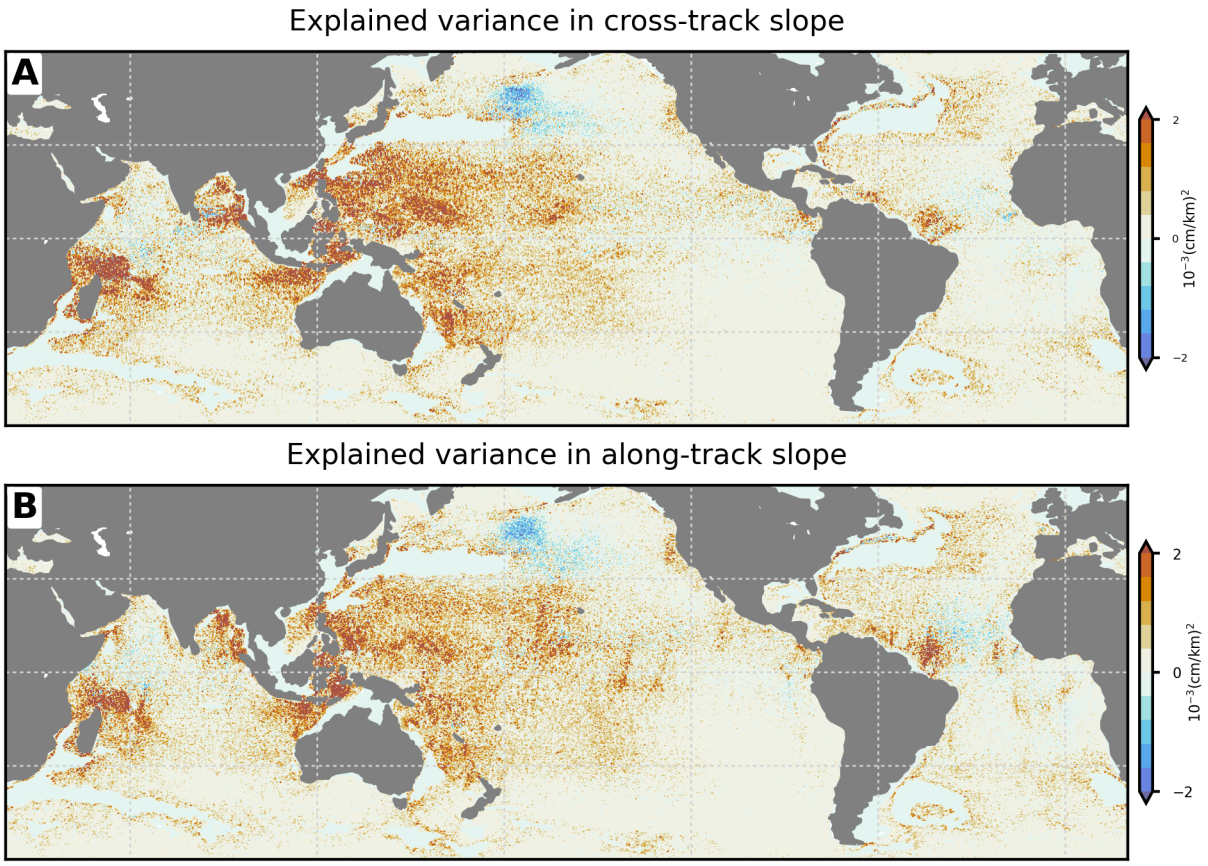

Figure S2: **HYCOM's skill in representing the slopes of non-phase-locked semidiurnal internal tides.** The panels quantify the explained variance in SWOT observations by HYCOM for the non-phase-locked internal tide slope components: (**A**) cross-track and (**B**) along-track. Areas of high explained variance (red) signify successful model capture of incoherent slope signals. Conversely, negative values (blue) indicate poor model-observation agreement where the predicted signal changes oppose the observed changes. Regions dominated by strong mesoscale eddy contamination, which complicates the robust separation of these signals, were entirely masked out.

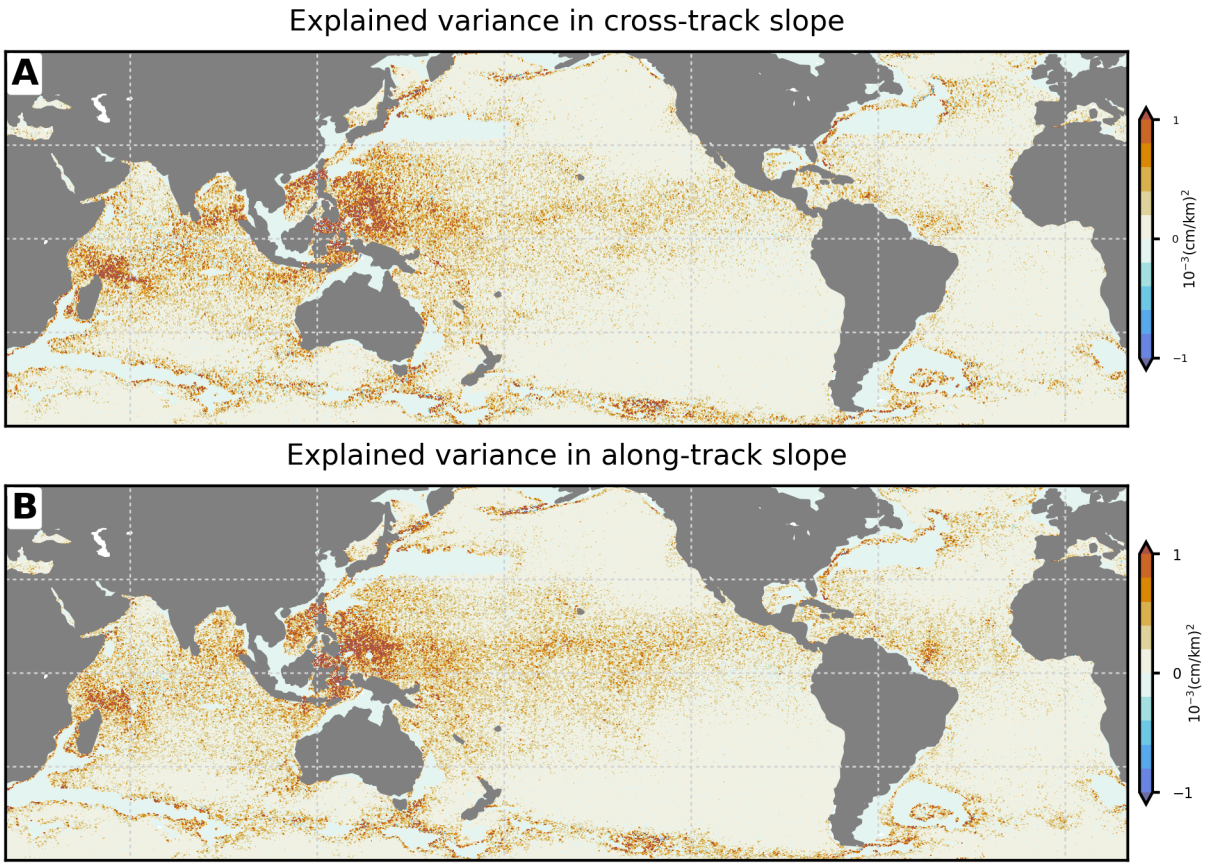

Figure S3: **Same as Fig. S2 but for the diurnal internal tide.**

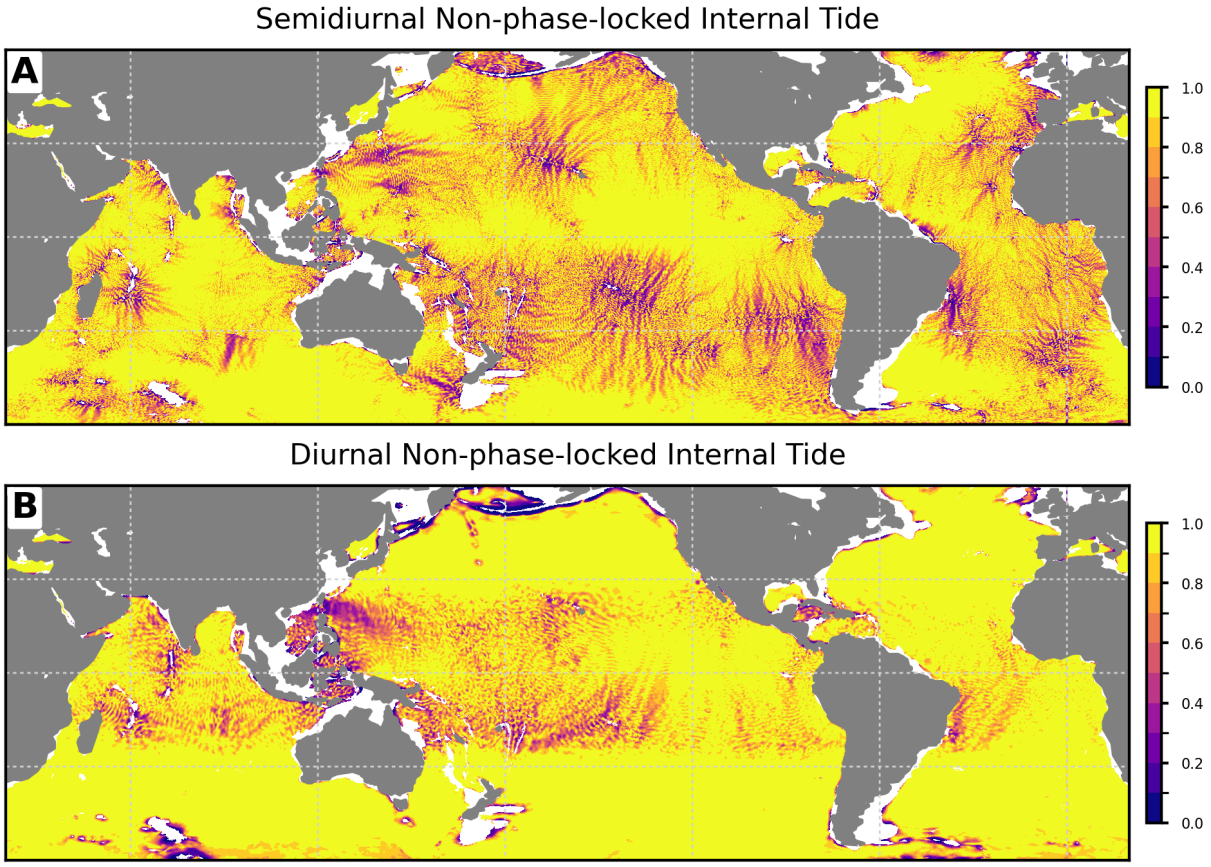

Figure S4: **Incoherent internal tides dominate regional variance.** Fraction of the total internal tide variance contributed by the non-phase-locked (incoherent) component for the (**A**) semidiurnal and (**B**) diurnal frequency bands, simulated by HYCOM. Regions where the fraction approaches 1 indicate that incoherent dynamics dominate the local internal tide field, a phenomenon typically observed far from generation sites. Conversely, areas near 0 are dominated by the predictable, phase-locked internal tide.

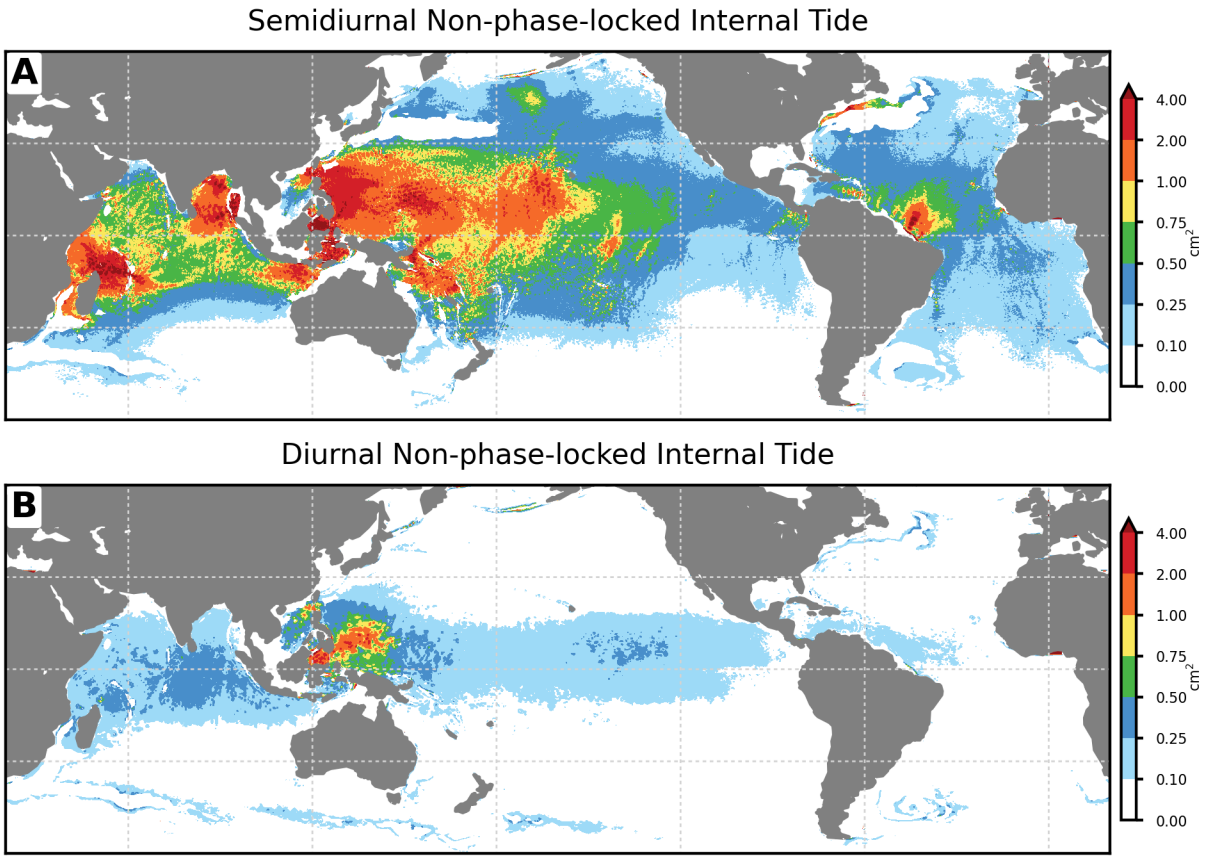

Figure S5: **The global footprint of non-phase-locked internal tides.** Absolute variance (in cm^2) of the non-phase-locked (incoherent) internal tide signal for the (**A**) semidiurnal and (**B**) diurnal frequency bands, simulated by HYCOM. Energetic hotspots (red) are concentrated nearby major generation topography. The maps illustrate the magnitude and broad spatial extent of these stochastic tidal signals as they propagate and dissipate across ocean basins.

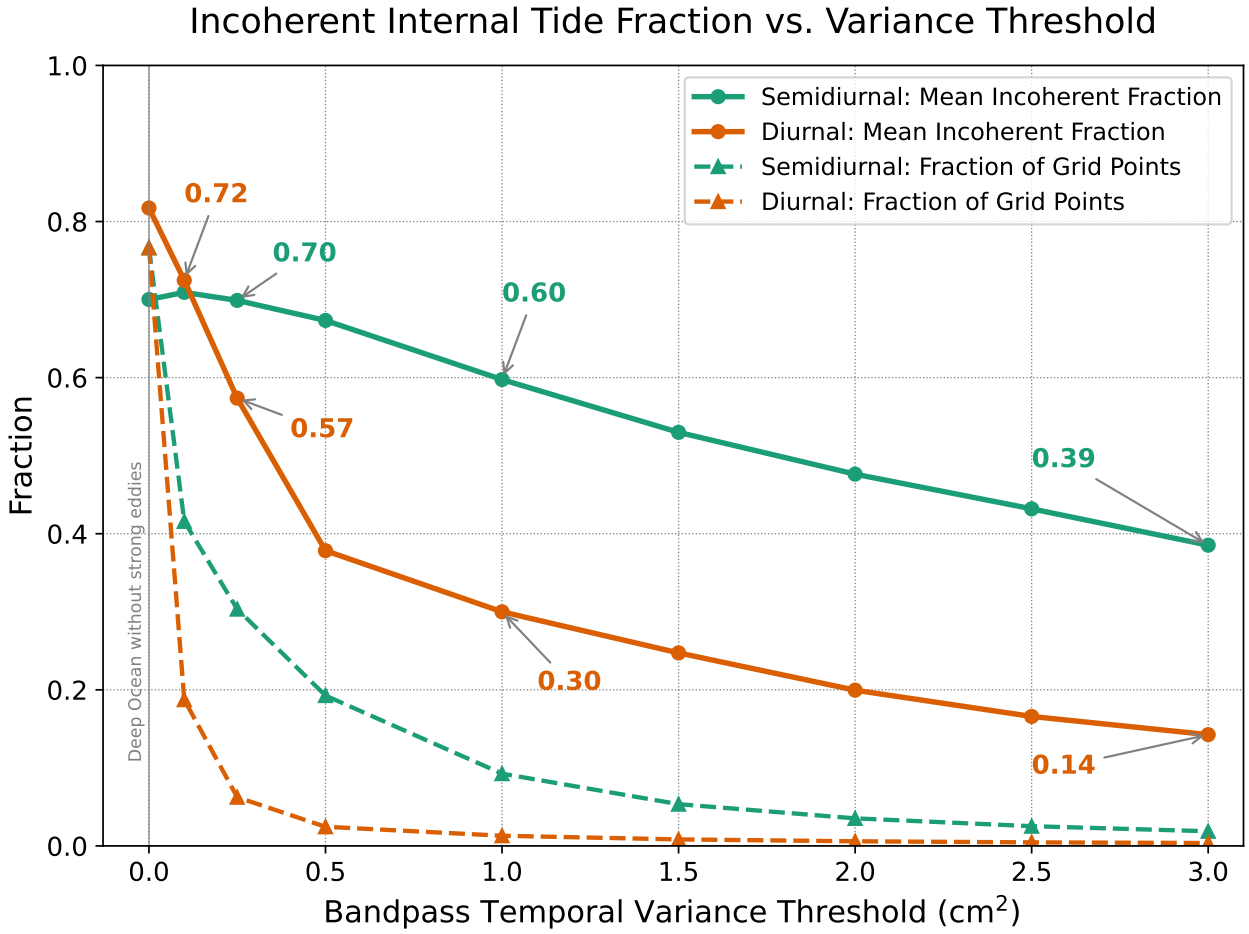

Figure S6: **Persistence of non-phase-locked internal tides across energy thresholds in the global ocean.** Solid lines show the global mean fraction of internal tide energy that is non-phase-locked (incoherent) for semidiurnal (teal) and diurnal (orange) frequency bands, plotted as a function of increasing temporal variance threshold (i.e., as analysis focuses on the most energetic grid points). Dashed lines represent the fraction of ocean grid points exceeding each threshold value. Results reveal that even when only the strongest internal tide regions are considered, a large portion of the internal tide energy remains non-phase-locked—indicating the prevalence and persistence of temporally modulated internal tides throughout the world ocean.

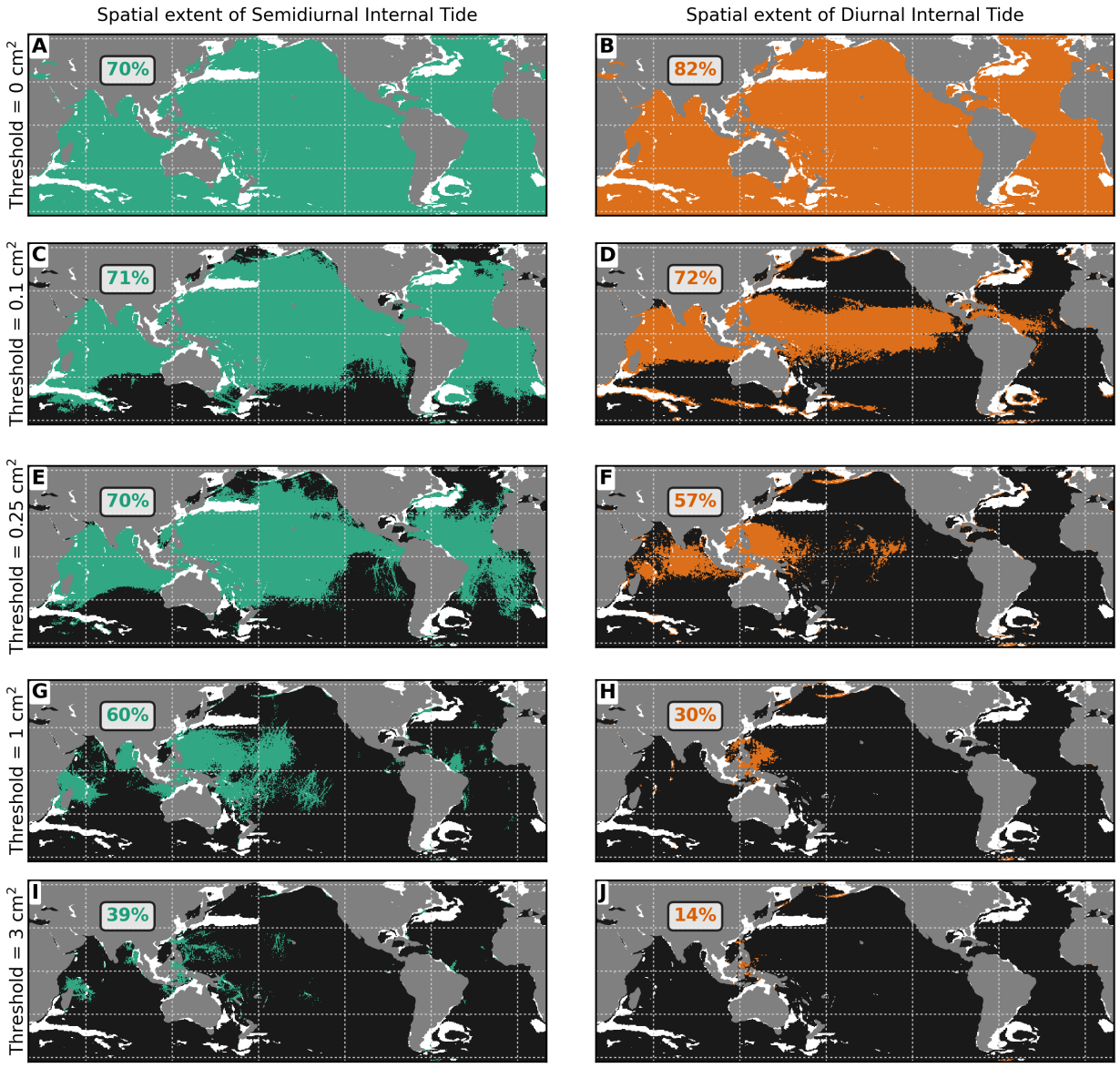

Figure S7: **The global footprint of non-phase-locked internal tides.** Global maps showing the ocean regions where total internal tide variance exceeds specific thresholds, from 0 to 3 cm^2. The analysis is shown for the (**A**, **C**, **E**, **G**, **I**) semidiurnal and (**B**, **D**, **F**, **H**, **J**) diurnal frequency bands. Colored areas meet the variance threshold specified for each row, while black areas fall below it. White regions are masked due to strong mesoscale eddies where the separation of non-phase-locked internal tides is difficult. The percentage in each panel indicates the mean fraction of the total variance contributed by the non-phase-locked (incoherent) component, averaged over the colored regions shown.

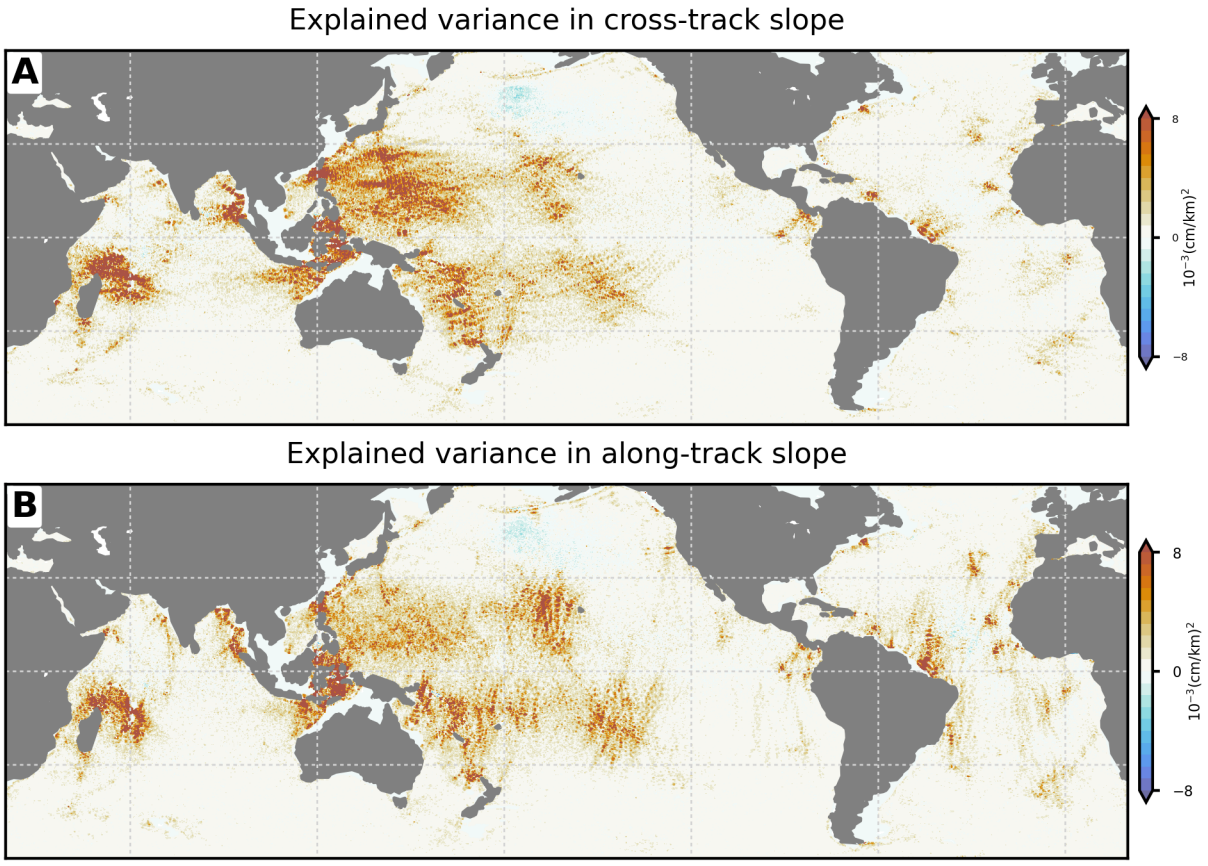

Figure S8: **Same as Fig. S2 but for the total internal tide signal including both phase-locked and non-phase-locked components.**

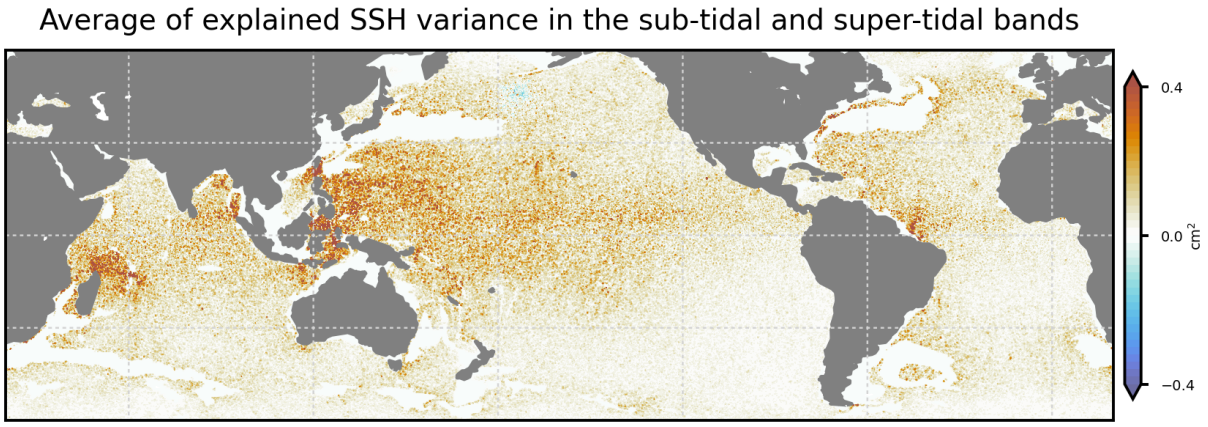

Figure S9: **Estimate of non-tidal variance leakage into the semidiurnal band.** Global map showing the average explained variance in the sub-tidal and super-tidal frequency bands. This metric serves as an estimate of the noise-floor, representing potential leakage from mesoscale eddies into the semidiurnal internal tide band.